Supporting Information

Electro-Optically Tunable Multifunctional Metasurfaces

Ghazaleh Kafaie Shirmanesh,[†] Ruzan Sokhoyan,[†] Pin Chieh Wu, [†,‡] and Harry A. Atwater[†,ᵍ,*]

[†] Thomas J. Watson Laboratory of Applied Physics and [ᵍ] Kavli Nanoscience Institute, California Institute of Technology, Pasadena, California 91125, USA

[‡] Department of Photonics, National Cheng Kung University, Tainan 70101, Taiwan

[*]E-mail: haa@caltech.edu

1. Comparison to the previously proposed design

In our previous paper,[1] a dual-gated Al-based metasurface was used, while, in the new design, a single-gated Au-based metasurface is presented. In the design presented in our previous paper, all metasurface elements were connected together and the same bias voltage was applied to all of them. However, the new metasurface operates by individually controlling each metasurface pixel. This requires the metasurface pixels to be electronically isolated. The requirement of individually-addressable metasurface elements makes the single-gated metasurface easier to be fabricated compared to its dual-gated counterpart.

In the proposed single-gated metasurface, the lower dielectric layer acts as an optical dielectric, removing the limitation of using HAOL as the lower dielectric layer. Replacing the HAOL layer by a lower index dielectric (Al_2O_3) resulted in a higher reflectance minimum.

In addition, the proposed Au-based metasurface can provide a smaller amplitude modulation accompanied by a phase shift comparable to the single-gated Al-based metasurface. This supports the operating principle of the multifunctional metasurface that mainly relies on the phase modulation. Figure S1 illustrates the amplitude and phase shift of the Al-based and Au-based metasurfaces as a function of applied biases. As can be seen, the proposed metasurface can provide a more modest amplitude modulation with an elevated reflectance minimum level compared to the previous metasurface design.

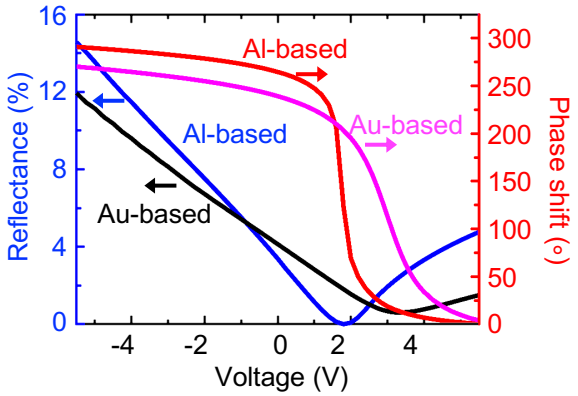


Figure S1. Reflectance and phase shift as a function of applied bias for the new design compared with the previous dual-gated metasurface design.[1]

2. Calculating electrostatic properties of ITO

In order to calculate the optical response of metasurfaces under applied bias, we first need to extract the properties of the ITO layer. To this end, we obtained the spatial distribution of charge carriers in the ITO layer by coupling finite difference time domain optical simulations (FDTD Lumerical) with device physics simulations (Device Lumerical). In our device physics calculations, the assumed parameters for ITO were obtained from our previous work.[1] Once the spatial distributions of charge carriers under different applied biases were identified, we calculated the complex dielectric permittivity of ITO ε_{ITO} by using the Drude model.[1] Figure S2a-c show the simulated spatial distribution of charge carrier concentration, real and imaginary part of the permittivity of ITO for different applied biases. As can be seen in Figure S2b, by changing the applied bias, an epsilon near zero (ENZ) region is observed within the ITO layer, at a region close to the interface of the ITO and HAOL film.

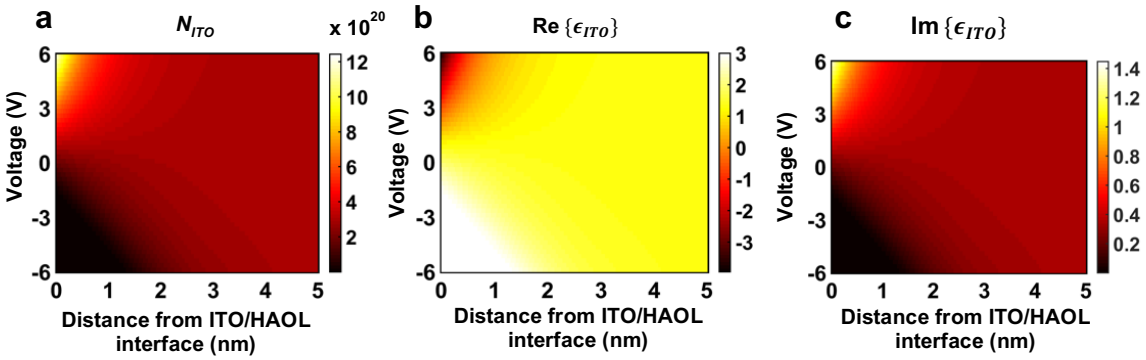


Figure S2. Calculated spatial distribution of (a) charge carrier density, (b) real and (c) imaginary part of the permittivity of ITO for different applied biases.

3. Full-wave simulation of reconfigurable metasurface

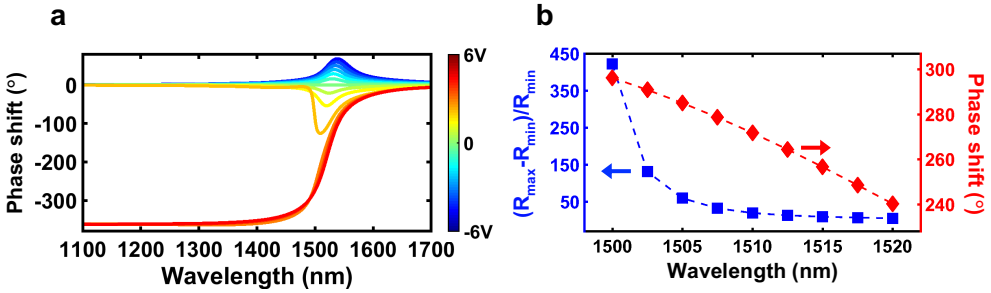


Figure S3. (a) Simulated phase shift spectrum for different applied biases. The phase shift was calculated with respect to the phase of the reflection from the metasurface without applied voltage. (b) Maximum achievable reflectance change (square) and phase modulation (diamond) at different wavelengths.

To gain further insight, we analyzed the electromagnetic fields in the metasurface at the resonance wavelength. The spatial distribution of the electric field intensity, under an applied bias of -6V, 0V, and +6V are presented in Figure S4a-c. Zoomed-in images of the electric field inside the dielectric spacer of the metasurface, consisting of the Al_2O_3/ITO/HAOL heterostructures are shown in the insets. As can be seen, at the applied bias of +6V, there will be a strong field enhancement in the accumulation region of the ITO layer which occurs subsequent to the existence of ENZ condition in the mentioned layer. By leveraging this strong field enhancement in the active region of the ITO layer, the complex permittivity change can be drastically emphasized.

Our electromagnetic calculations show that the metasurface phase and amplitude tunability is based on an interplay between magnetic plasmon resonance and the ENZ region of ITO. To show this, the amplitude of the magnetic field inside the metasurface is shown in Figure S5. The field distributions are presented at different wavelengths and under different applied biases. As can be seen in Figure S5d-f, at the resonance wavelength λ = 1510 nm, there exists a large-magnitude magnetic field that is localized in the gap region between gold antenna and gold back plane.

Figure S6 shows the spatial distribution of the z-component of the electric field within the metasurface under different applied biases. As can be seen, the z components of the electric field around the right and left edges of the antenna are antiparallel to each other. This antiparallel field, accompanied by the curl of the current density is consistent with large magnetic field shown in

Figure S5d-f, indicating that the considered resonance is a magnetic plasmon resonance. We note that the strength of the magnetic dipole is strongly modified by altering the applied bias.

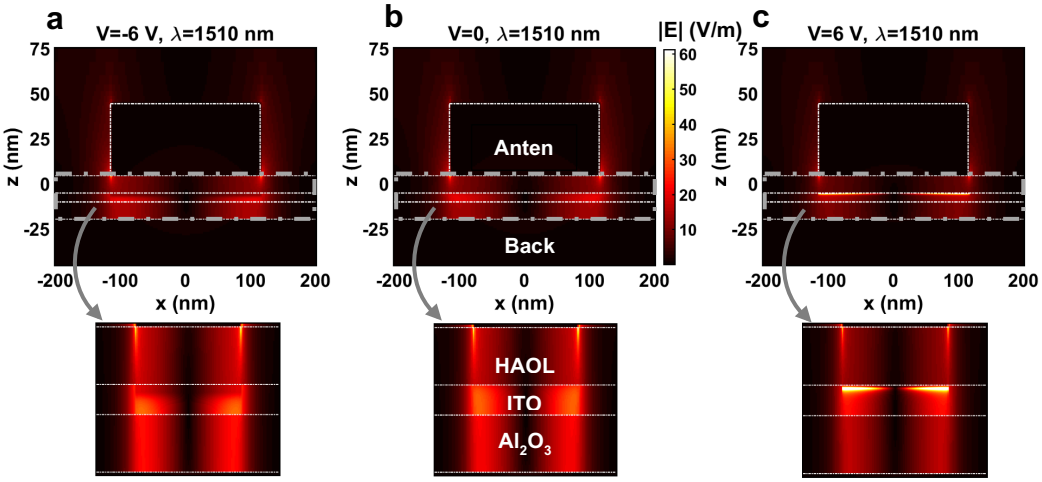


Figure S4. Spatial distribution of the amplitude of the electric field at the operating wavelength of λ = 1510 nm for different voltages of (a) V = -6 V, (b) V = 0, and (c) V = 6 V. The insets show the zoomed-in image of the Al_2O_3/ITO/HAOL nano-sandwich.

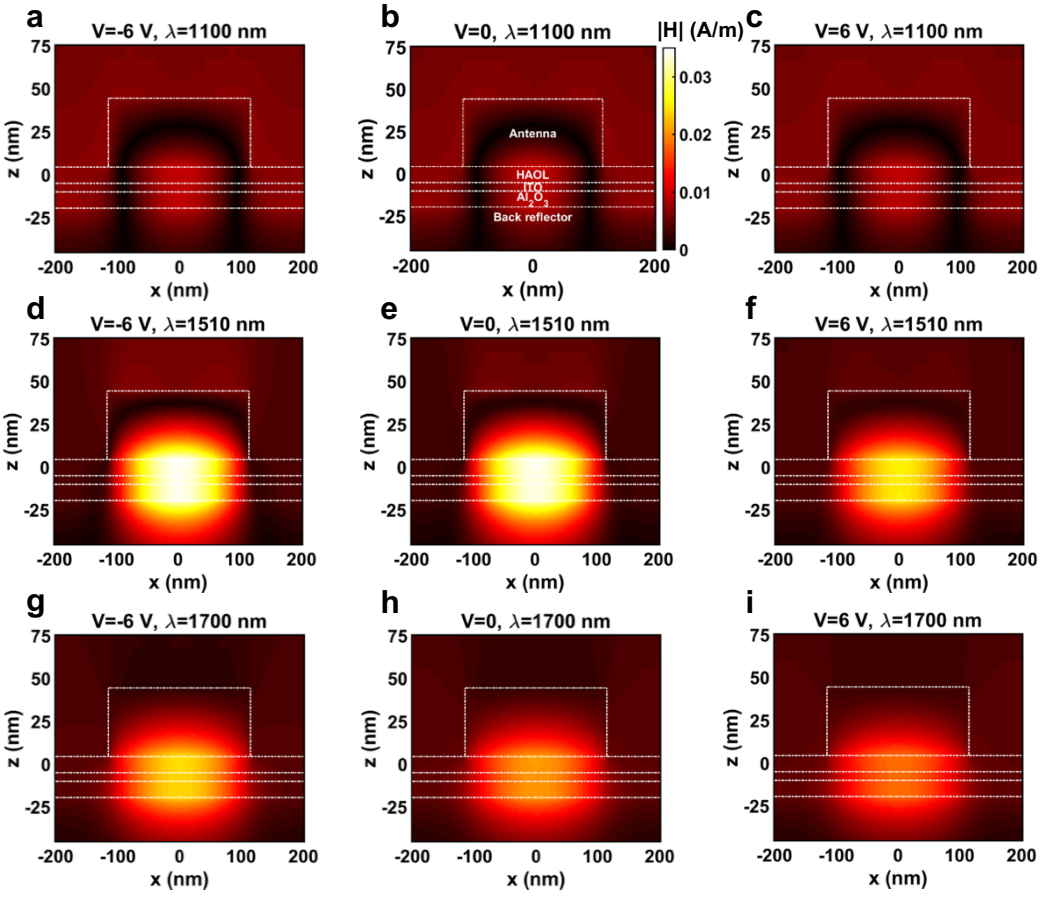


Figure S5. Spatial distribution of the amplitude of the magnetic field at the operating wavelength of (a-c) λ = 1100 nm, (d-f) λ = 1510 nm, and (g-i) λ = 1510 nm for different voltages of V = -6 V (a, d, and g), V = 0 (b, e, and h), and V = 6 V (c, f, and i).

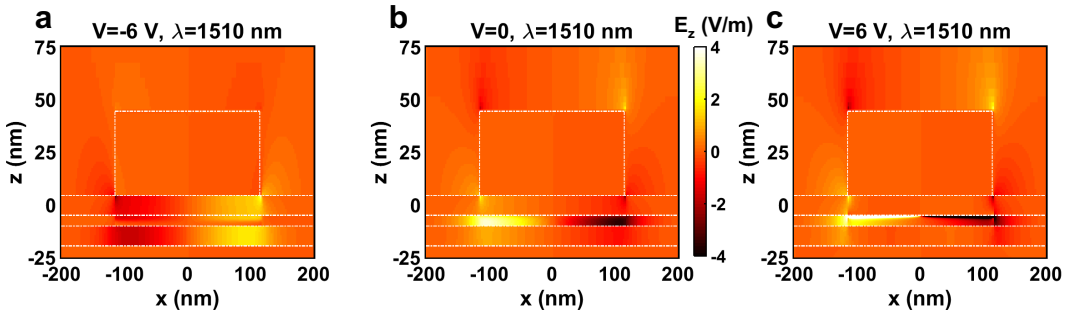


Figure S6. Spatial distribution of the z-component of the electric field at the wavelength of λ = 1510 nm, under applied bias (a) V = -6 V, (b) V = 0, and (c) V = 6 V.

4. Increasing metasurface reflectance level

Due to the strong field confinement in the ITO layer of the metasurface at ENZ condition, which is indeed the operation principle of the modulation provided by the metasurface, these plasmonic active metasurfaces show small reflectance values. It should be noted that in the proposed tunable metasurface, one can always see a tradeoff between the amplitude of the reflection from the metasurface and the maximum achievable phase shift.

Figure S7 shows how changing the thickness of different layers could increase the reflectance value at the cost of decreasing the phase shift. Figure S7a shows the reflectance spectrum for different antenna thicknesses for the unbiased case (see Figure S7b for a zoomed in presentation at the resonant vicinity). Figure S7c presents the spectrum of the maximum achievable phase shift defined by

$$\text{Max. phase shift} = \text{Acquired phase (V} = 6\text{V)} - \text{Acquired phase (V} = -6\text{V)} \quad \text{(S1)}$$

As can be seen, increasing the thickness of the antennas could increase the unbiased reflectance level to some extent. While further increasing the antenna thickness will result in a higher reflectance, it will drastically decrease the maximum achievable phase shift. The same tradeoff can be observed when increasing the thickness of the lower dielectric layer and the ITO layer for which reflectance (maximum achievable phase shift) spectra are depicted in Figure S7d,e (Figure S7f) and Figure S7g,h (Figure S7i), respectively.

Another method to alter the reflectance from the metasurface is to cover the antennas by a dielectric layer. Figure S7j,k show the unbiased reflectance from the metasurface for different thicknesses of a SiO_2 layer covering the metasurface area. The maximum achievable phase shift spectrum is depicted in Figure S7l. As can be seen, increasing the thickness of the top SiO_2 layer up to 80 nm, would increase the reflectance from the metasurface. However, a 120 nm-thick SiO_2 layer will drastically decrease the maximum achievable phase shift. It should be noted that the dimensions of the antenna and the electrode are adjusted to l_a = 210 nm, w_a = 115 nm, and w_e = 130 nm such that the resonance wavelength of the metasurface when covered by an 80 nm-thick SiO_2 layer is the same as that of the original metasurface.

In addition to changing the metasurface physical dimensions, replacing the ITO layer by transparent conducting oxides with higher electron mobilities such as CdO, is expected to increase the reflectance level of the metasurface. However, investigating this would be beyond the scope of this paper.

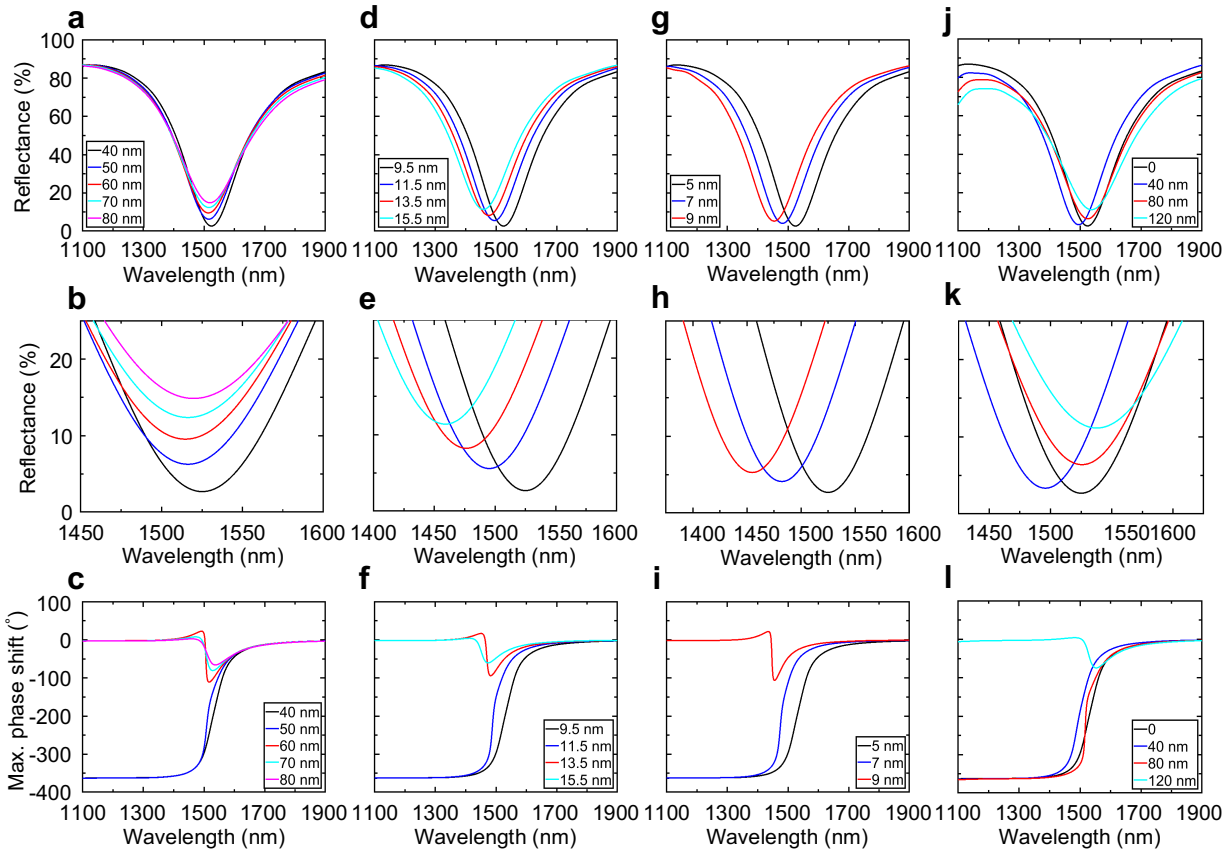


Figure S7. Effect of different layers of the tunable metasurface on reflectance and maximum achievable phase shift of the metasurface. (a) Reflectance spectrum, (b) zoomed-in image of the reflectance spectrum, and (c) maximum achievable phase shift for different antenna thickness values. (d) Reflectance spectrum, (e) zoomed-in image of the reflectance spectrum, and (f) maximum achievable phase shift for different lower Al_2O_3 thickness values. (g) Reflectance spectrum, (h) zoomed-in image of the reflectance spectrum, and (i) maximum achievable phase shift for different ITO thickness values. (j) Reflectance spectrum, (k) zoomed-in image of the reflectance spectrum, and (l) maximum achievable phase shift for different top SiO_2 thickness values.

5. Multifunctional metasurface fabrication

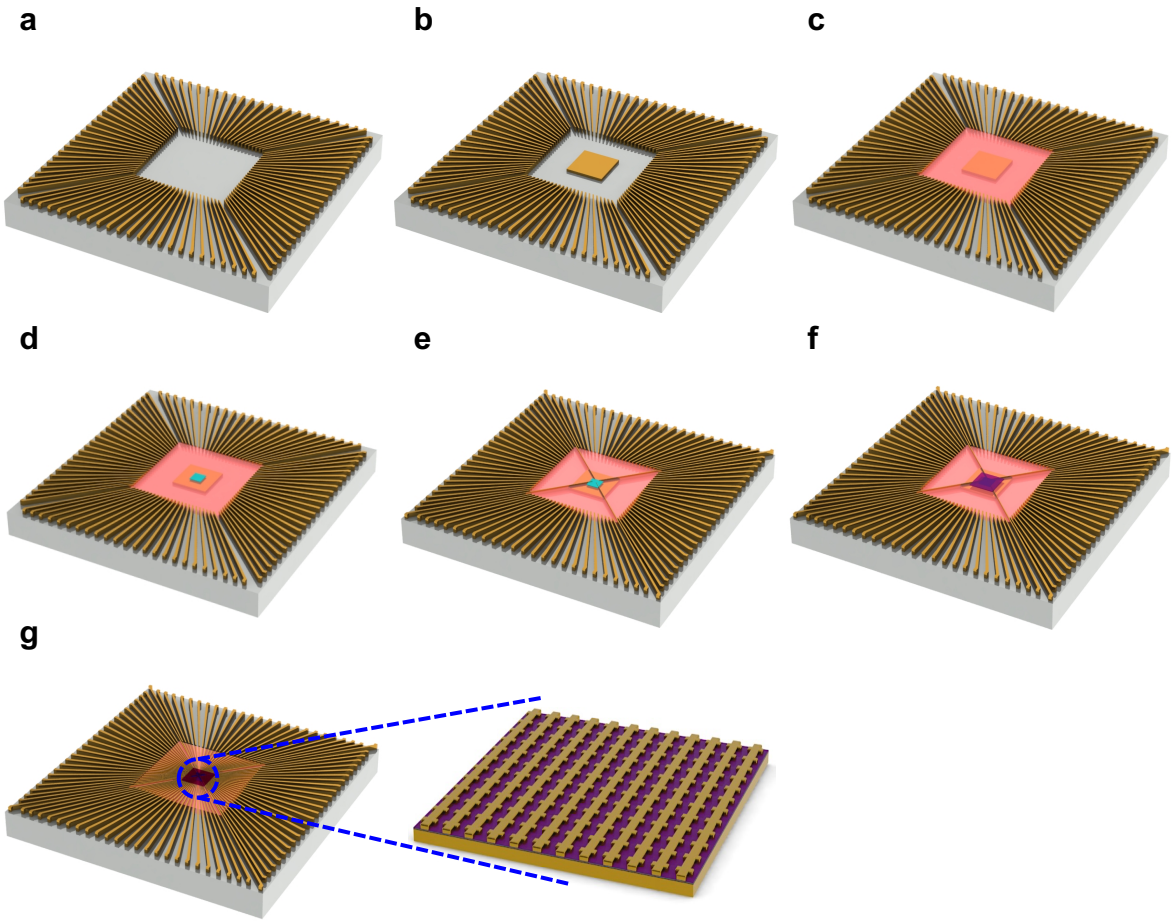


Figure S8. Sample fabrication steps. (a) Patterning the outermost connecting pads; (b) patterning the back reflector; (c) deposing the Al_2O_3 layer; (d) patterning the ITO layer; (e) patterning the connecting pads of the ITO layer; (f) depositing the HAOL gate dielectric; and (g) patterning the antenna array and the inner connecting pads.

6. Universal measurements setup

In order to measure all the functions performed by our multifunctional metasurface, we designed and built a custom optical measurement setup. This measurement setup is capable of measuring reflectance spectrum, phase shift, beam steering and reconfigurable focusing. Figure S9 shows our custom-built setup. Each measurement is performed through a part of our universal setup that are discussed in detail in the following sections. For all measurements, we utilized an uncollimated white light source from a halogen lamp (LA) and a visible CMOS image sensor camera (V-C) to visualize the sample surface.

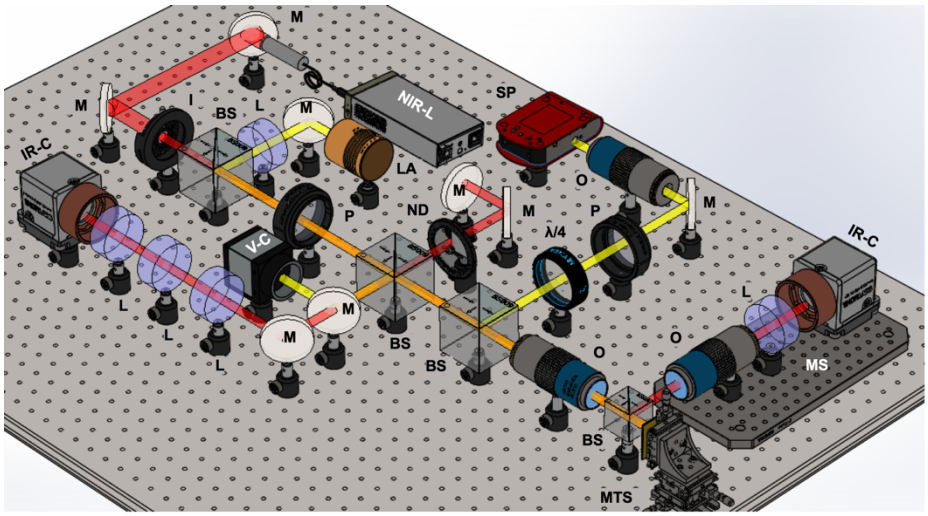


Figure S9. Universal measurement setup used for reflectance, phase shift, beam steering, and focusing measurements. NIR-L: NIR laser, M: mirror, I: iris, BS: 50:50 beam splitter, L: lens, LA: lamp, P: polarizer, ND: neutral density filter, λ/4:quarter-wave plate, SP: spectrometer, O: objective lens, MTS: metasurface sample, IR-C: IR CCD camera, V-C: visible CCD camera, MS: 2-axis motorized stage.

7. Reflectance measurements

Figure S10 shows the part of the universal optical setup that was used for reflectance measurements. For reflectance measurement, the surface of the metasurface sample was illuminated by an uncollimated white light from a halogen lamp (LA). The incident light was focused by an objective (O) with a long working distance (Mitutoyo M Plan Apo 20×, NA = 0.40, WD = 20 mm) after passing through a polarizer (P) and a 50:50 non-polarizing beam splitter (BS). Then the beam reflected from the metasurface was guided to a spectrometer *via* a beam splitter (BS) and a mirror (M). The reflectance was then obtained *via*

$$Reflectance\,[\%] = 100 \times \frac{R_{sample} - R_{dark}}{R_{reference} - R_{dark}} \quad \text{(S2)}$$

where R_{sample} is the raw reflectance from the metasurface sample, $R_{reference}$ is the raw reflectance from a mirror, and R_{dark} is the background reflectance in the absence of incident laser beam.

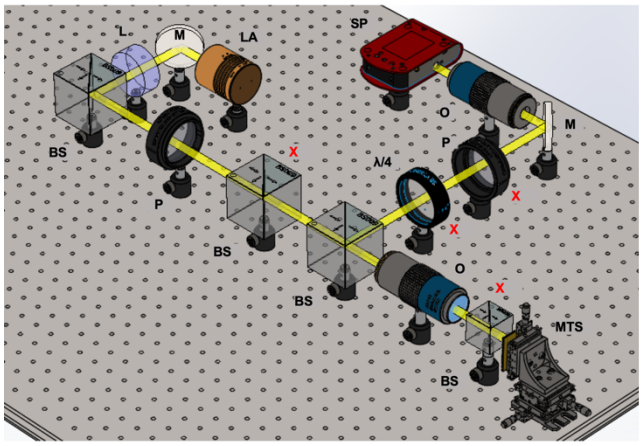


Figure S10. Optical setup used for reflectance measurement. LA: lamp, M: mirror, L: lens, BS: 50:50 beam splitter, P: polarizer, O: objective lens, MTS: metasurface sample, λ/4:quarter-wave plate, SP: spectrometer. The components indicated with red cross marks belong to the universal setup and are not used in this part of the measurement.

8. Phase shift measurements

In order to measure the reflection phase shift from the metasurface sample, we used a part of the measurement setup, shown in Figure S11. In this part of the setup, the metasurface sample was illuminated by a tunable NIR laser. The laser beam illuminated the metasurface after passing through an iris (I), a 50:50 non-polarizing beam splitter (BS), and an objective (O) with a long working distance (Mitutoyo M Plan Apo 20×, NA = 0.40, WD = 20 mm). The polarization of the incident beam was controlled by a polarizer (P) to make sure that the incident electric field was in the direction of the antennas.

The reflection from the sample was then directed towards an infrared camera (IR-C) by using the mentioned beam splitter (BS). In addition to the reflection from the metasurface sample, the laser beam, which served as a reference beam, was also guided to the camera by using mirrors (M). The phase shift of the reflection was then calculated using the method discussed in our previous work.[1]

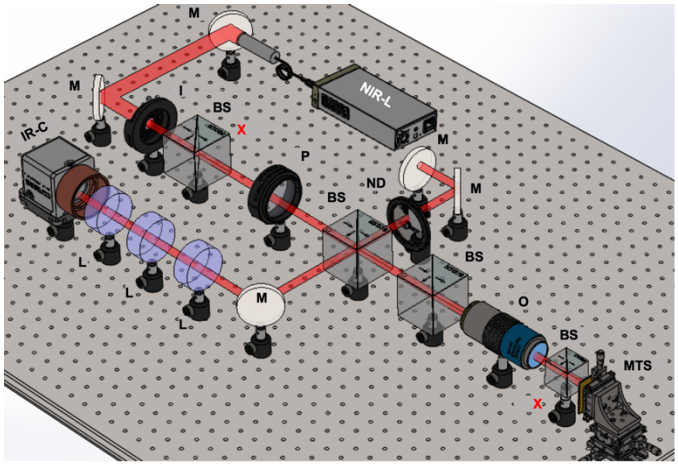


Figure S11. Optical setup used for phase shift measurement. NIR-L: NIR laser, M: mirror, I: iris, BS: 50:50 beam splitter, P: polarizer, ND: neutral density filter, O: objective lens, MTS: metasurface

sample, L: lens, IR-C: IR CCD camera. The components indicated with red cross marks belong to the universal setup and are not used in this part of the measurement.

9. Beam steering measurements

In order to perform beam steering measurement, we measured the far-field radiation pattern of the sample in the Fourier space by using the setup shown in Figure S12. In this part of the setup, a coherent beam from a tunable NIR laser illuminated the metasurface sample. The laser beam was focused on the sample by an objective (O) with a long working distance (Mitutoyo M Plan Apo 20×, NA = 0.40, WD = 20 mm) after passing through an iris (I), a polarizer (P), and a 50:50 non-polarizing beam splitter (BS). The reflected beam was then guided to an IR camera (IR-C) positioned in the Fourier plane, and the radiation pattern was captured.

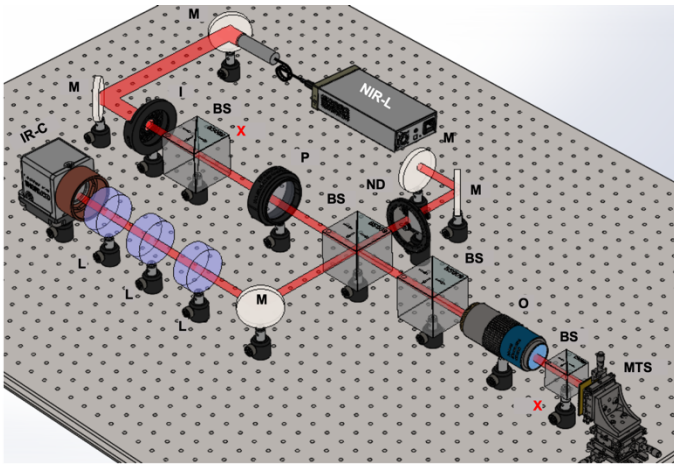


Figure S12. Optical setup used for beam steering measurement. NIR-L: NIR laser, M: mirror, I: iris, BS: 50:50 beam splitter, P: polarizer, O: objective lens, MTS: metasurface sample, L: lens, IR-C: IR CCD camera. The components indicated with red cross marks belong to the universal setup and are not used in this part of the measurement.

10. Reconfigurable focusing measurements

In order to measure the reconfigurable focusing performance of the metasurface, we used a part of the universal setup depicted in Figure S13. In this setup, the metasurface sample was illuminated by a coherent beam from a tunable NIR laser. The laser beam was directed to the sample surface by passing through an iris (I), a polarizer (P), an objective (O) with a long working distance (Mitutoyo M Plan Apo 20×, NA = 0.40), and a 50:50 non-polarizing beam splitter (BS). The reflected beam from the metasurface was then captured by an imaging system. The imaging system consisted of an infrared camera (IR-C), and an objective lens (O) with long working distance (Mitutoyo M Plan Apo 20×, NA = 0.40, WD = 20 mm) paired with a tube lens. The imaging system was then moved from the image plane by a 2-axis motorized stage (MS), that could move in the *x* and *y* directions with a resolution of 100 nm, and the intensity profile of the reflected beam in the *xy*-plane was captured at different depths.

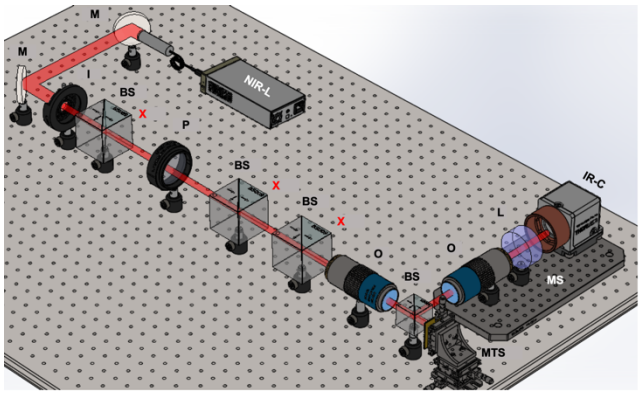


Figure S13. Optical setup used for focusing performance measurement. NIR-L: NIR laser, M: mirror, I: iris, BS: 50:50 beam splitter, P: polarizer, O: objective lens, MTS: metasurface sample, L: lens, IR-C: IR CCD camera, MS: 2-axis motorized stage. The components indicated with red cross marks belong to the universal setup and are not used in this part of the measurement.

11. Choosing the number of metasurface pixels

In order to implement beam steering, we needed to find the number of metasurface elements that need to be individually controlled. Figure S14 shows the efficiency of the beam steering for different numbers of metasurface elements. In this case, the 4-level phase profile and a repetition number of $RN = 3$ (corresponding to the green curve in Figure 4a in the main manuscript) were used. As one can see, increasing the number of metasurface elements will decrease the width of the first diffraction order. However, increasing the number of metasurface elements will increase the surface area of the metasurface, leading to a higher probability of the gate dielectric breakdown due to the existence of pinholes. Besides, increasing the number of individually-controllable metasurface elements will increase the number of pads to be wire-bonded, hence elevate the complexity of the device fabrication. Here, we chose to use 96 different metasurface elements to be independently controlled. As can be seen in Figure S14, this number of metasurface pixels would provide a satisfying beam steering performance.

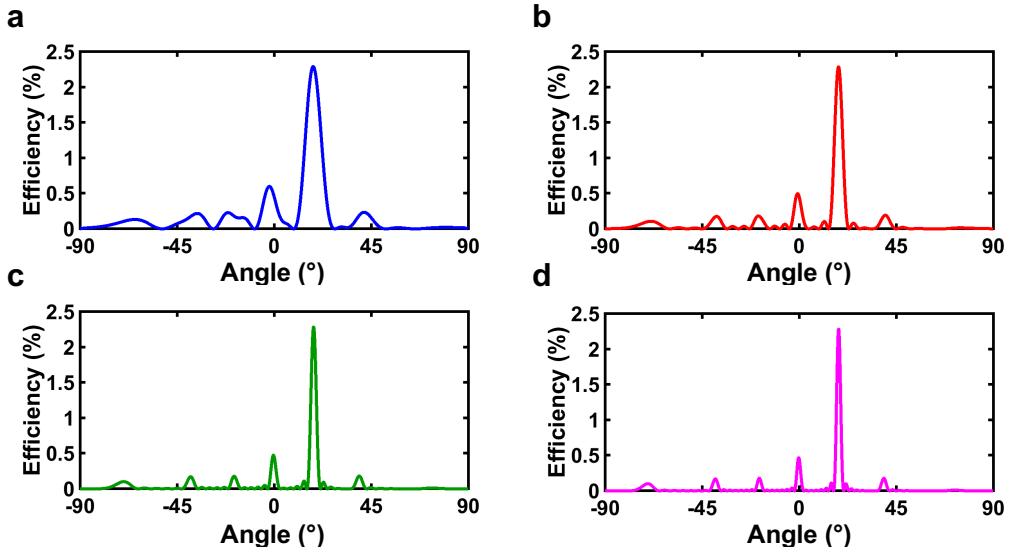


Figure S14. Beam steering efficiency for different numbers of individually-controllable metasurface elements (*N*). (a) *N* = 24, (b) *N* = 48, (c) *N* = 72, and (d) *N* = 96.

12. Beam steering metasurface simulations

In order to theoretically study the beam steering performance of the metasurface, we first performed full-wave electromagnetic simulations using FDTD Solutions Lumerical. To this end, we created a constant phase gradient along the metasurface, effectively creating a periodic phase pattern that could provide us specific steering angles. The phase values were adopted from the unit cell simulations for each applied bias. Figure S15a shows spatial phase profile of the beam steering metasurface for different repetition numbers (*RN*). The far field radiation patterns of the metasurface obtained from the full-wave simulation can be seen in Figure S15b. Each curve represents the radiation pattern corresponding to the spatial phase profile illustrated with the same color depicted in Figure S15a. As can be seen, the metasurface is capable of providing a maximum steering angle of 70.5° when *RN* = 1.

After fabricating the metasurface, we noticed a pitch size difference between the designed metasurface and the fabricated device due to fabrication non-idealities. In order to take this pitch difference into account, we used an analytical formulation to calculate the far field pattern of the beam steering metasurface by using a blazed grating approach. In this approach, we used the framework of antenna array theory.[1] With the reflected beam being steered in the *z*-*x* plane, the far-field intensity at an observation angle θ with respect to *z*-axis, using the Fraunhofer approximation, can be given by:

$$I(\theta) = |E_{patt}|^2 \times |AF|^2, \tag{S3}$$

where $I(\theta)$ is the far-field intensity, E_{patt} is the far-field radiation pattern of a single metasurface element, and *AF* is the array factor that can be given as

$$AF = \sum_{j=1}^{N} \sqrt{R_j} e^{i((j-1)\, k\, d \sin(\theta)+\Phi_j)}. \tag{S4}$$

Here, *j* numerates the metasurface element, and *N* denotes the total number of elements that scatter light with a given phase, hereafter referred to as emitters. *k* denotes the free space wavenumber $k = 2\pi/\lambda$, and *d* gives the distance between neighboring emitters. R_j and Φ_j are the reflectance and phase shift of the j^{th} emitter. In this approach, we set $|E_{patt}| = 1$ because of the relatively omnidirectionality of our emitters. As a result, only the array factor is analyzed.

By implementing this method using the simulated reflectance and phase shift values, we obtained the far field radiation pattern of the beam steering metasurface, illustrated in Figure S15c. Here, we used blaze gratings consisting of four metasurface elements with phase shifts of 0^o, 90^o, 180^o, 270^o. As can be seen, there is a good agreement between the analytically-obtained radiation patterns and the full-wave simulation results. Once we confirmed the ability of our analytical formulation in predicting the far field radiation pattern, we employed the same method by using the dimensions obtained from the SEM images to calculate the far field pattern of our fabricated meta-device (Figure S15d).

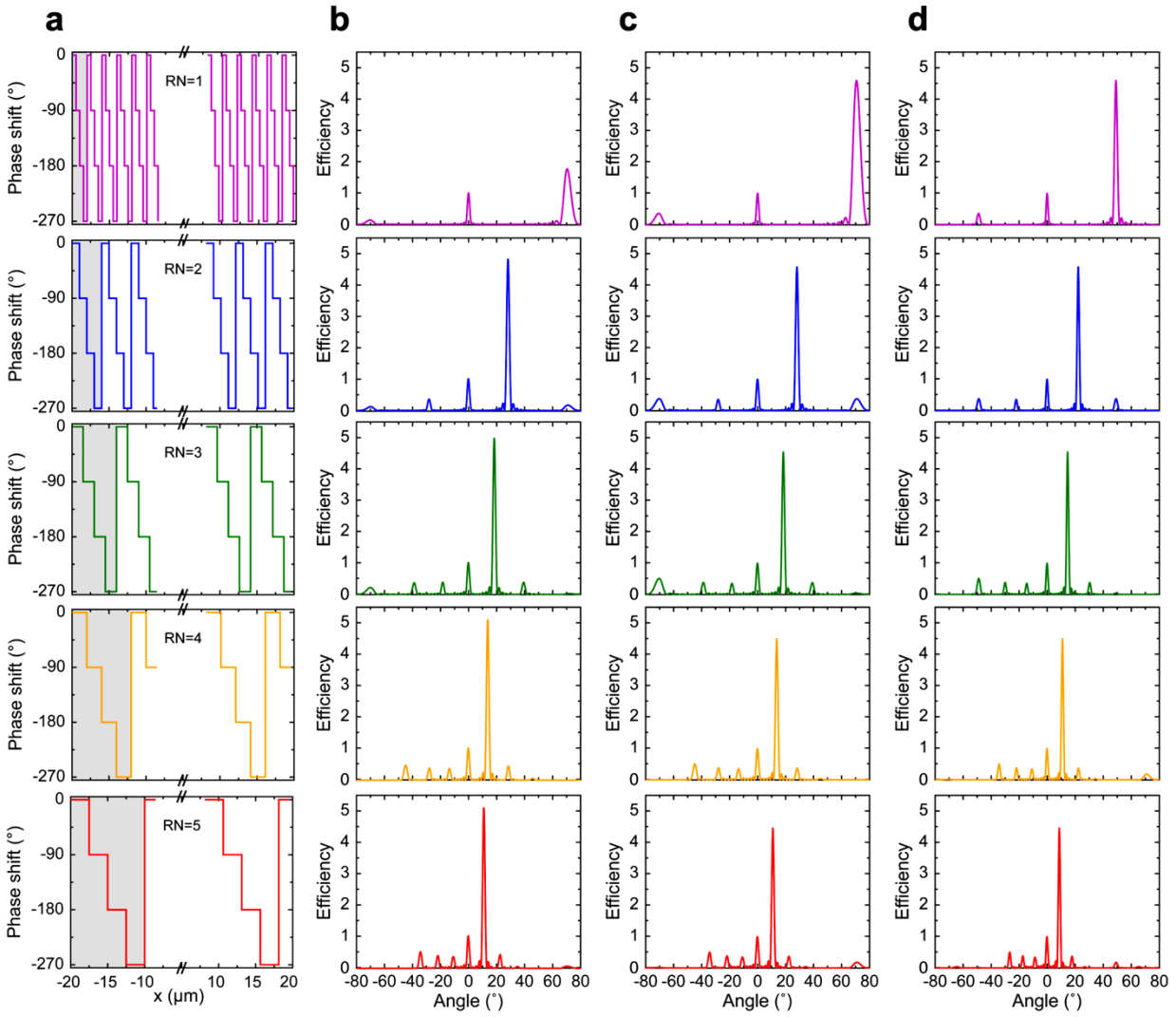


Figure S15. (a) Spatial phase distribution of the beam steering metasurface with different repetition number (*RN*) values. (b) Full-wave simulation results of the beam steering metasurface for p = 400 nm and λ = 1510 nm. Simulation results of the beam steering metasurface obtained through analytical calculations for (c) p = 400 nm, λ = 1510 nm and (d) p = 504 nm, λ = 1522 nm.

Generally speaking, active metasurfaces rely on "on-resonant" operation. In our case, the operation wavelength is located around the resonance dip (Figure 2c of main manuscript). When applying an external bias, we perturb the resonance characteristics that results in a phase shift. However, besides the phase shift, we also observe reflectance modulation. Hence, when performing beam steering by using the metasurface, the amplitude of the light scattered by each metasurface element depends on the applied bias voltage. This undesired amplitude modulation significantly deteriorates the beam steering performance of our metasurface. Figure S16 illustrates the analytical simulation results of the beam steering performance for the case of equal amplitudes for all metasurface pixels for different *RN* values (Figure S16a-f). The phase shift values are obtained from Figure 2e of the main manuscript. The beam steering simulation results for the practical metasurface in which the amplitudes are modulated when changing the applied bias voltage are presented in Figure S16g-l. The reflectance and phase shift values were obtained from Figure 2d and Figure 2e of the main manuscript, respectively. As seen in Figure S16, the unequal reflectance

values of different metasurface pixels that are generated as a result of amplitude modulation when changing the applied bias, create unwanted lobes in the far field pattern, while keeping the steered angle and bandwidth unchanged. In other words, the ratio of the reflected light intensity at the desired angle to that of the undesired angles (quantified by the beam directivity[2]) is drastically decreased due to the variation of the amplitude.

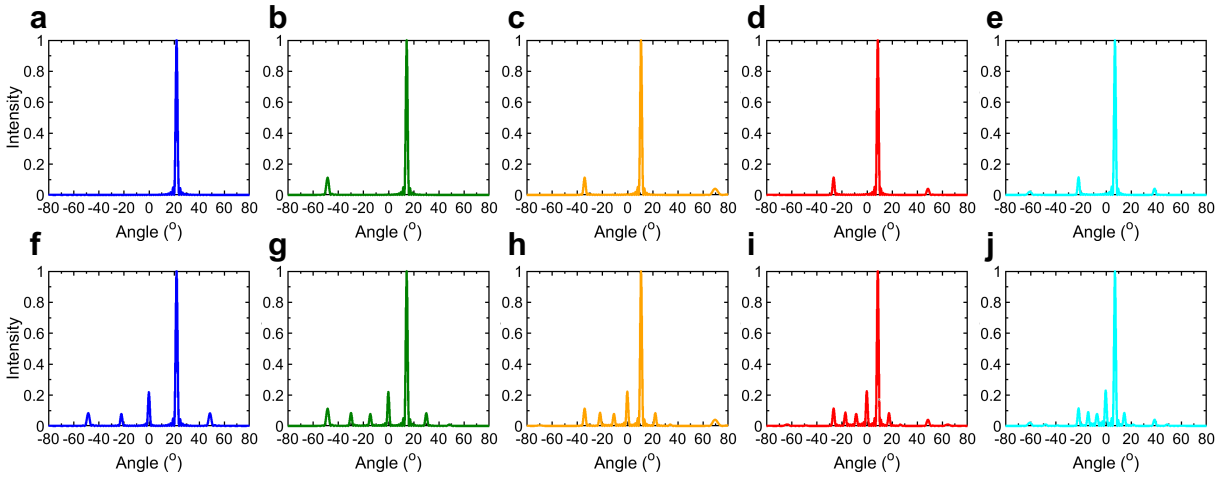


Figure S16. Effect of amplitude and phase modulation on the far field radiation pattern of the beam steering metasurface. Simulation results of the beam steering metasurface obtained through analytical calculations when equal reflectance values and step phase distributions were assumed for all metasurface pixels when (a) *RN* = 2, (b) *RN* = 3, (c) *RN* = 4, (d) *RN* = 5, and (e) *RN* = 6. Analytical simulation results of the beam steering metasurface with unequal reflectance values and step phase distribution for different metasurface pixels when (f) *RN* = 2, (g) *RN* = 3, (h) *RN* = 4, (i) *RN* = 5, and (j) *RN* = 6.

Another importance factor that needs to be taken into account is the detailed choice of the phase profile across the metasurface that can significantly influence the beam steering characteristics. Ideally, when steering a beam to a steering angle θ_0, the wave reflected form the metasurface should be a plane wave such that its wavefront is tilted with respect to the metasurface plane by an angle θ_0. To achieve an ideal tilted plane wave, one uses the following phase profile across the metasurface: $\varphi_{ideal}=(j\text{-}1)\ k\ p\ sin(\theta_0)$, where j numerates the metasurface element, p is the metasurface period, k is the wavenumber of the incoming plane wave.[3] To experimentally realize this phase profile, we need to be able to access phase shifts spanning from 0° to 360°. However, in our metasurface, the maximal accessible phase shift is limited to values around 270°. To implement beam steering by using our multifunctional metasurface, we approximate the ideal phase profile φ_{ideal} by stairstep profiles shown in Figure 4a. As seen in Figure 4b,c, the designed step profiles enable beam steering. One could also realize beam steering by appropriately choosing the period of the phase profile and linearly changing the phase within the period until reaching the maximal value of 270°.

For the ultimate clarity, we plot a period for these three different phase profiles (ideal, step profile, linear) in the case of a steering angle of 14.6° (Figure S17). In Figure S17, the dots correspond to the phase values at spatial positions where the metasurface elements are located while the solid lines show the phase profiles effectively created across the metasurface. The stairstep phase profile shown in Figure S17 corresponds to the following spatial distribution of

phases (0°, 0°, 0°, -90°, -90°, -90°, -180°, -180°, -180°, -270°, -270°, -270°). Note that the stairstep phase profile shown in Figure S17 is identical to the one shown in the second panel of Figure 4a.

To generate the linear phase profile, the desired steering angles were chosen to be the same as the ones demonstrated by applying stairstep phase profiles. As a result, for each steering angle, the number of metasurface pixels (*MP*) in one supercell was chosen to be $MP = 4 \times RN$ to ensure that the lengths of the generated supercells using linear phase profiles are identical to those used in the stairstep case. Accordingly, the phases within a supercell were picked to be evenly spaced between 0° and -270°. In other words, the phase shift between metasurface elements within a supercell was chosen as $270°/(4 \times RN - 1)$. As an example, here, we set a constant phase shift between neighboring metasurface elements as 270/11 corresponding to the case of *RN*=3. In case of the linear phase profile, the supercell is given as (0, -24.5455°, -49.0909°, -73.6364°, -98.1818°, -122.7273°, -147.2727°, -171.8182°, -196.3636°, -220.9091°, -245.4545°, -270°). For all considered phase profiles (ideal, stairstep, and linear) the supercell incorporates 12 metasurface pixels, and the length of the supercell (or, equivalently, the period of the generated blazed grating) is 4.8 μm. The designed stairstep profile attempts to accurately reproduce both the period and the slope of the ideal phase profile. On the other hand, the slope of the linear phase profile deviates from the slope of the ideal phase profile.

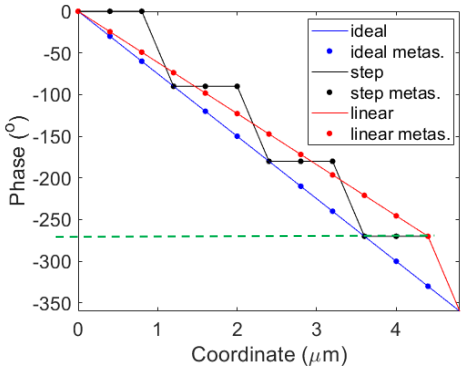


Figure S17. A supercell for a steering angle of 14.6°. Blue line corresponds to the 'ideal' phase profile, red line to the linear phase profile while the black line represents the stairstep phase profile used in the present work. The horizontal green dashed line indicates the maximal achievable phase shift in our metasurface.

As a next step, we calculate far field radiation patterns in the cases when linear phase profiles were employed to create the supercells. The far field radiation patterns for linear phase profiles that correspond to different MP values are presented in Figure S18a-e. Our simulation results show that employing linear phase profiles leads to slightly better beam steering performance. As seen in Figure S18a-e, linear phase profiles yield smaller sidelobes at negative angles as compared to the case of the stairstep profiles. On the other hand, the linear phase profiles generate larger undesired sidelobes at positive angles. Moreover, for smaller steering angles (larger supercell sizes), programming the microcontrollers to provide small voltage increments that could lead to linearly distributed phase profiles would be much more complicated compared to the cases when 4-level phase distributions are used. As a result, in our experimental demonstration, we used 4-level stairstep phase profiles with different *RN* values in order to change the size of the supercell and accordingly access different steering angles.

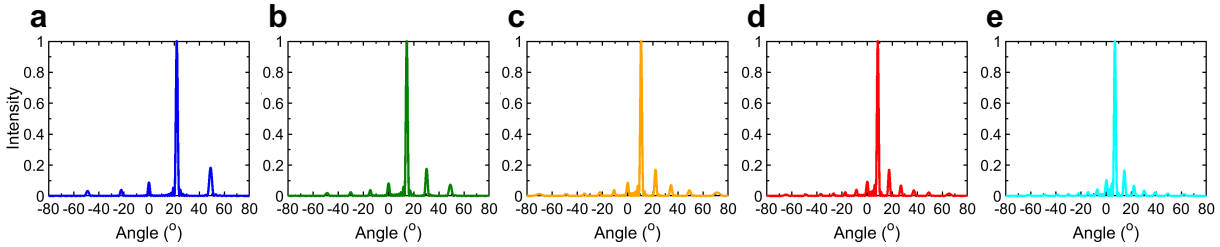


Figure S18. Simulation results of the beam steering metasurface obtained when unequal reflectance values and linear phase distributions were assumed for all metasurface pixels for (a) *MP* = 8, (b) *MP* = 12, (c) *MP* = 16, (d) *MP* =20, and (e) *MP* = 24.

As can be implied from Figure S16 and Figure S18, to improve the beam directivity, one has to minimize the amplitude variation when applying electrical bias to the metasurface element. This could be achieved by increasing the number of external control knobs, which can be used to actively control the phase of a metasurface pixel.[1, 4] Increasing the maximally achievable phase shift could also improve the beam steering performance of the metasurface since in that case one can use the 'ideal' phase profile to steer the beam (Figure S18).

13. Spatial phase and voltage profiles for reconfigurable focusing meta-mirror

In order to demonstrate focusing, we designed the spatial phase profile of the metasurface pixels such that the beams reflected from individual pixels are in phase at the desired focal point. To this end, the phase shift provided by the metasurface is dictated by the hyperboloidal profile:

$$\phi(x) = -\frac{2\pi}{\lambda}\left(\sqrt{f^2 + x^2} - f\right) \tag{S5}$$

where λ is the wavelength, f is the focal length and x is the distance of the pixel from the center of the lens.

Figure S19 shows the spatial phase profile of focusing meta-mirrors designed to have focal length of $f = 1.5$ µm (Figure S19a), $f = 2$ µm (Figure S19b), and $f = 3$ µm (Figure S19c). The square points show the ideal required phase values obtained from equation (S5) and the diamond points represent the phase values acquired by the metasurface obtained from phase measurements (see Figure 2d of the main manuscript). After fitting the measured phase values to the ideal curves, we obtained the voltage values corresponding to the fitted phase profiles. Figure S19d-f show the spatial voltage profile of the focusing meta-mirrors with focal length of $f = 1.5$ µm, $f = 2$ µm, and $f = 3$ µm.

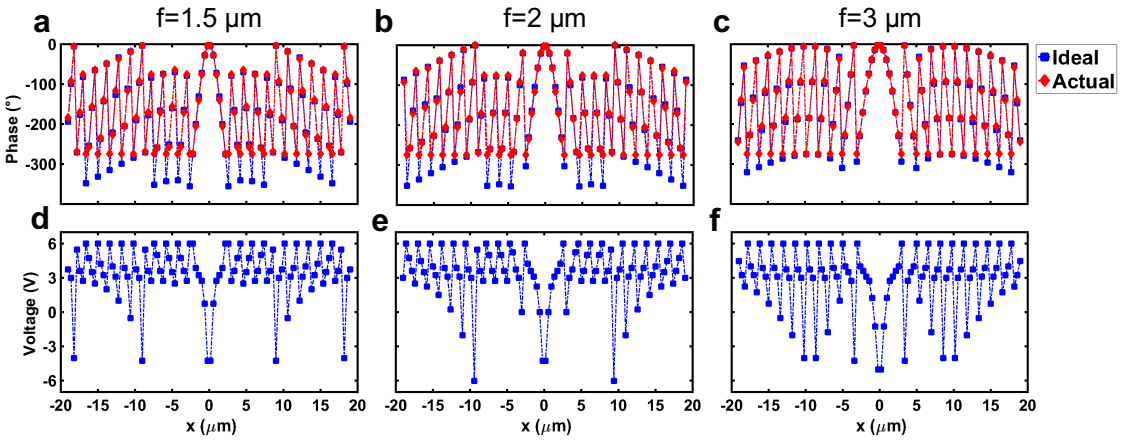


Figure S19. Spatial phase distribution of focusing meta-mirror with focal lengths of (a) f = 1.5 μm, (b) f = 2 μm, and (c) f = 3 μm. Square points show the ideal phase values and diamond points present the phase values acquired by the metasurface. Spatial voltage distribution of focusing meta-mirror with focal lengths of (d) f = 1.5 μm, (e) f = 2 μm, and (f) f = 3 μm.

14. Reconfigurable focusing meta-mirror: accessing longer focal lengths

Figure S20a-c show the spatial distribution of the phase shift (diamond) and the corresponding applied bias voltage (square) required to focus the reflected beam at the focal lengths of 15 μm, 20 μm and 25 μm. The voltage distribution was designed using the measured bias voltage/phase relationship (Figure 2d of main manuscript). The measured intensity profiles mapped in the *xz*-plane are illustrated in Figure S20d-f.

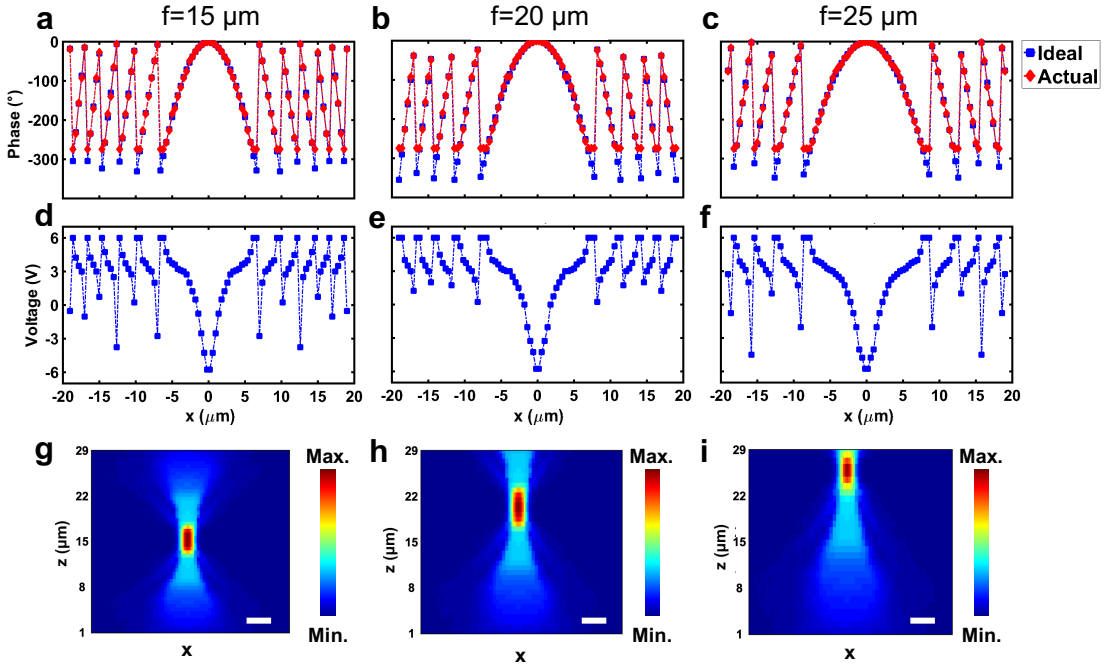


Figure S20. Spatial phase distribution of focusing meta-mirror with focal lengths of (a) f = 15 μm, (b) f = 20 μm, and (c) f = 25 μm. Square points show the ideal required phase values and diamond points present the phase values acquired by the metasurface. Spatial voltage distribution of focusing meta-mirror with focal lengths of (d) f = 15 μm, (e) f = 20 μm, and (f) f = 25 μm. Measured intensity profile

of the beam reflected from the focusing meta-mirror with focal lengths of (g) f = 15 μm, (h) f = 20 μm, and (i) f = 25 μm. Scale bar is 2 μm.

As can be seen, our universal metasurface is able to provide tunable focusing with reconfigurable focal lengths only by reprogramming the voltages applied to the metasurface. The focal length can be tuned from small values and can be extended to large ones. We can further increase the focal length of the metasurface by increasing the number of metasurface pixels that are individually controlled. Figure S21 shows the spatial phase profile and the corresponding voltage profile of the focusing metasurface with focal length as large as f = 150 μm (Figure S21a,d), f = 200 μm (Figure S21b,e), and f = 250 μm (Figure S21c,f). The focusing meta-mirrors with the phase/voltage profiles presented in Figure S21 consist of 288 individually-addressable metasurface pixels. Such tunable focusing meta-mirror with micro-scale focal length can be potentially applied in many applications, such as light-field imaging[5] and full-color imaging.[6]

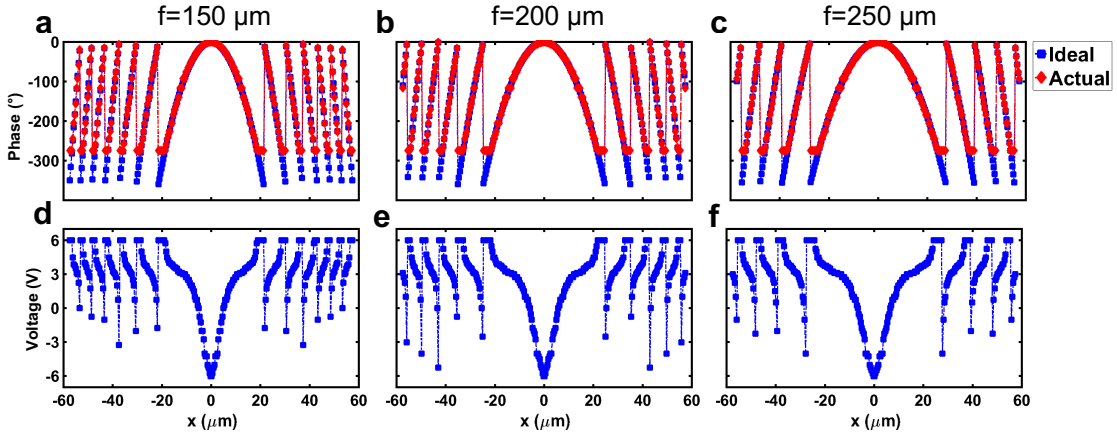


Figure S21. Spatial phase distribution of focusing meta-mirror with focal lengths of (a) f = 150 μm, (b) f = 200 μm, and (c) f = 250 μm. Square points show the ideal required phase values and diamond points present the phase values acquired by the metasurface. Spatial voltage distribution of focusing meta-mirror with focal lengths of (d) f = 150 μm, (e) f = 200 μm, and (f) f = 250 μm.

Reference

1. Shirmanesh, G. K.; Sokhoyan, R.; Pala, R. A.; Atwater, H. A., Dual-Gated Active Metasurface at 1550 nm with Wide (>300°) Phase Tunability. *Nano Lett.* **2018,** *18*, 2957–2963.
2. C. A. Balanis, Fundamental Parameters and Figures-of-Merit of Antennas. In *Antenna Theory: Analysis and Design*, Edition 3, John Wiley & Sons: New York, 1997. Chapter 2, pp 44-57.
3. Engstrom, D.; Bengtsson, J.; Eriksson, E.; Goksor, M, Improved Beam Steering Accuracy of a Single Beam with a 1D Phase-Only Spatial Light Modulator. *Op. Express* **2008**, 16, 18275-18287.
4. Han, S.; Kim, S.; Kim, S.; Low, T.; Brar, V. W.; Jang, M. S., Complete Complex Amplitude Modulation with Electronically Tunable Graphene Plasmonic Metamolecules. *ACS Nano* **2020**, 14, 1166-1175.
5. Lin, R. J.; Su, V.-C.; Wang, S.; Chen, M. K.; Chung, T. L.; Chen, Y. H.; Kuo, H. Y.; Chen, J.-W.; Chen, J.; Huang, Y.-T.; Wang, J.-H.; Chu, C. H.; Wu, P. C.; Li, T.; Wang, Z.; Zhu, S.; Tsai, D. P., Achromatic Metalens Array for Full-Colour Light-Field Imaging. *Nat. Nanotechnol.* **2019**, 14, 227–231.
6. Wang, S.; Wu, P. C.; Su, V.-C.; Lai, Y.-C.; Chen, M.-K.; Kuo, H. Y.; Chen, B. H.; Chen, Y. H.; Huang, T.-T.; Wang, J.-H.; Lin, R.-M.; Kuan, C.-H.; Li, T.; Wang, Z.; Zhu, S.; Tsai, D. P., A Broadband Achromatic Metalens in the Visible. *Nat. Nanotechnol.* **2018**, 13, 227–232.